Multifeature-Based High-Resolution Palmprint Recognition

Jifeng Dai and Jie Zhou, *Senior Member*, *IEEE*

Abstract—Palmprint is a promising biometric feature for use in access control and forensic applications. Previous research on palmprint recognition mainly concentrates on low-resolution (about 100 ppi) palmprints. But for high-security applications (e.g., forensic usage), high-resolution palmprints (500 ppi or higher) are required from which more useful information can be extracted. In this paper, we propose a novel recognition algorithm for high-resolution palmprint. The main contributions of the proposed algorithm include the following: 1) use of multiple features, namely, minutiae, density, orientation, and principal lines, for palmprint recognition to significantly improve the matching performance of the conventional algorithm. 2) Design of a quality-based and adaptive orientation field estimation algorithm which performs better than the existing algorithm in case of regions with a large number of creases. 3) Use of a novel fusion scheme for an identification application which performs better than conventional fusion methods, e.g., weighted sum rule, SVMs, or Neyman-Pearson rule. Besides, we analyze the discriminative power of different feature combinations and find that density is very useful for palmprint recognition. Experimental results on the database containing 14,576 full palmprints show that the proposed algorithm has achieved a good performance. In the case of verification, the recognition system's False Rejection Rate (FRR) is 16 percent, which is 17 percent lower than the best existing algorithm at a False Acceptance Rate (FAR) of 10^{-5}, while in the identification experiment, the rank-1 live-scan partial palmprint recognition rate is improved from 82.0 to 91.7 percent.

Index Terms—Palmprint, orientation field, the composite algorithm, density map, data fusion.

1 Introduction

Palmprint recognition has considerable potential as a personal identification technique. Palmprints share most of the discriminative features with fingerprints and, in addition, possess a much larger skin area and other discriminative features such as principal lines. For access control usages, scanning the palmprint is not only fast but also highly acceptable for the public [1]. Palmprint recognition also has a significant role in forensic applications as about 30 percent of the latents recovered from crime scenes are from palms [2]. One of the most important goals of the FBI's Next Generation Identification System is to develop a national palmprint identification system [3].

Fig. 1 shows a typical palmprint image. There are two basic features in a palmprint: ridges and creases. Ridges are formed by the arrangement of the mastoid in the dermal papillary layer. They come into being during the three-to-four months of the fetal stage and are fixed in the adolescence stage [4]. The ridge pattern of the palm is unique for an individual, just like the finger tip [1]. But unlike the fingerprint, there are many creases in the palmprint. They can be further classified as immutable and mutable creases. Immutable creases mainly consist of three principal lines, namely, radial transverse crease, proximal transverse crease, and distal transverse crease. They divide the palmprint into three regions: thenar, hypothenar, and interdigital. Mutable creases mainly come from drying cracks, which come into being in Spring and Winter when the weather is dry and disappear when it is wet in Summer and Autumn [5]. These are also easily masked by compression and noise [6]. Both the principal lines and ridges are firmly attached to the dermis, and are immutable for the whole life [7].

Existing research on palmprint recognition mostly concentrates on low-resolution (about 100 ppi) images [9], [10], [11], [12], [13], [6], [14], which are mainly captured by contactless devices. For low-resolution images, palmprint ridges cannot be observed, and the matching is mainly based on crease and texture features. Shu and Zhang [15] extracted the hand shape and principal line features to build the palmprint recognition system. Zhang and Shu [16] presented the datum point invariance and line feature matching characteristics in palmprint verification. Duta et al. [17] tried to represent and match the principal lines with feature points which locate on the principal lines and are extracted by a series of morphological operations. You et al. [18] matched the principal lines by the interesting points, which are extracted by the Plessey operator [19]. In [9], Zhang et al. proposed a contactless low-resolution palmprint acquisition device using a CCD camera and a 2D Gabor phase encoding scheme is proposed to extract palmprint textures. In [6], Huang et al. highlighted the discriminative power of principal lines and used those to design a palmprint verification system. Sun et al. [20] proposed the ordinal palmprint representation and unified several low-resolution palmprint recognition algorithms into a framework. In [21], Yue et al. proposed a modified fuzzy C-means cluster algorithm for competitive code-based palmprint recognition. Kumar [22] integrated cohort

• *The authors are with the Department of Automation, Tsinghua University, Beijing 100084, China.*
E-mail: djf05@mails.tsinghua.edu.cn; jzhou@tsinghua.edu.cn.

Manuscript received 27 Oct. 2009; revised 1 Apr. 2010; accepted 26 June 2010; published online 19 Aug. 2010.
Recommended for acceptance by S. Prabhakar.
For information on obtaining reprints of this article, please send e-mail to: tpami@computer.org, and reference IEEECS Log Number TPAMI-2009-10-0721.
Digital Object Identifier no. 10.1109/TPAMI.2010.164.

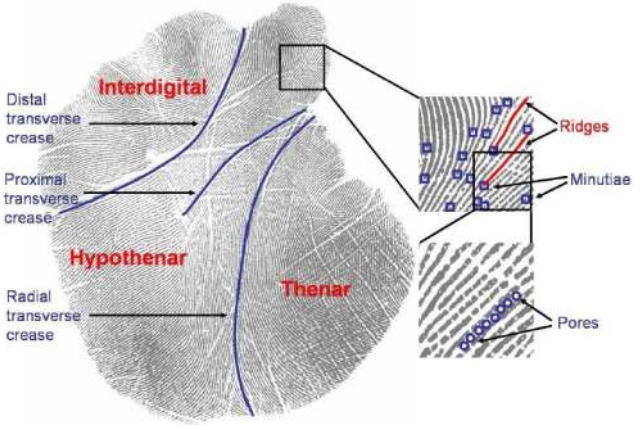

Fig. 1. The principal lines, regions, ridges, and minutiae in a palmprint [8].

information in the decision making and a better performance was reported.

But, for high-security applications (e.g., forensic usages), high-resolution palmprints are required in which the highly discriminative ridge feature [1] can be observed. Moreover, certain ridge patterns are acceptable in a court of law [23], which facilitates its use in forensic applications. Further, the prints lifted from a crime scene usually have poor quality and a complex background which warrants extraction of features in addition to texture in order to make a reliable identification.

The presence of a large number of creases is one of the major challenges in reliable extraction of the ridge information. Creases break the continuity of ridges, leading to a large number of spurious minutiae. Moreover, in regions having high crease density, the orientation field of the ridge pattern is obscured by the orientation of creases. In [8], a minutiae-based high-resolution palmprint recognition system achieving acceptable accuracy was recently reported by Jain and Feng. A region-growing algorithm was proposed which could extract the orientation field on palmprints in the presence of creases. And a novel minutia descriptor, MinutiaCode, was utilized. In the matching stage, the weighted sum of minutiae and orientation field similarities was calculated to measure the similarity between palmprints. The algorithm achieved a rank-1 recognition rate of 78.7 percent when searching live-scan partial palmprints on a background database containing 10,200 full palmprints.

In this paper, we propose a multifeature-based high-resolution palmprint recognition system in which minutiae, orientation field, density map, and principal line map are reliably extracted and combined to provide more discriminatory information. A novel orientation field estimation algorithm is proposed which is not significantly affected by the presence of creases. It can adaptively choose a suitable estimation method according to the qualities of different regions. A novel fusion scheme is also designed for identification applications. And it achieves a higher recognition rate than the conventional fusion methods, such as the weighted sum rule, SVMs, and Neyman-Pearson rule. In addition, we found that the density map feature is a good supplement to minutiae for palmprint recognition. The experimental results on a database containing 14,576 full palmprints from 13,736 unique palms indicate that the proposed method achieves a much better performance than the algorithm proposed in [8]. In verification experiments, the False Rejection Rate (FRR) is 17 percent lower than that obtained using the algorithm proposed in [8] when the False Acceptance Rate (FAR) is 10^{-5}. In the case of identification, the rank-1 live-scan partial palmprint recognition rate of our system reaches 91.7 percent, which is 9.7 percent higher than the case when Jain and Feng's technique is used.

The rest of this paper is organized as follows: In Section 2, the novel orientation field estimation algorithm is introduced. Section 3 describes the extraction of the other features. The features are fused by the proposed heuristic rule for identification usages and the conventional statistical learning methods for verification usages in Section 4. In Section 5, the experimental results are presented and analyzed. Finally, we finish with conclusions in Section 6.

2 The Composite Orientation Field Estimation

It is crucial for the palmprint recognition system to reliably estimate the orientation field. It is used in ridge enhancement and minutiae validation, making it very important in minutiae extraction. Various orientation estimation algorithms have been proposed for fingerprints [24], [25], [26]. These algorithms consist of two main steps: initial estimation and postsmoothing. Lots of postsmoothing methods have been designed, including the hierarchical gradient method [24], the model-based method [26], the region-growing algorithm [8], etc. But no matter how powerful these smoothing algorithms are, they all rely on the results provided by the initial estimation. If there are overwhelming errors in the initial estimation results, no smoothing algorithms can generate reliable results magically.

There are three commonly used initial estimation methods, namely, the gradient-based method [24], the discrete Fourier transform (DFT) [8], and the Gabor-filter-bank method [25]. The basic idea of the gradient-based method is that the ridge and valley can be seen as black-and-white stripes and the ridge's direction is perpendicular to the gradient direction. As for the Fourier transform method, it assumes that sine waves can effectively represent the black-and-white stripes, so the peak in the frequency domain of a local area corresponds to the central lines of the stripes in the image. The Gabor-filter-bank method shares the same basic assumption with the Fourier transform method. In the frequency domain, the Gabor-filter-bank method multiplies the frequency spectrum of the local area with a series of Gabor filters and selects the direction of the Gabor filter with the strongest response as the local ridge direction. This method is very time-consuming and is not suitable for processing prints with a large image size or online applications.

The above-mentioned methods perform well on the prints with few creases. But they cannot reliably estimate the orientation of palmprints with many creases. Basically, they focus on the change of grayscale and treat the black and white stripes equally, so the direction information of the black and white stripes would both influence the result. If there are no or few creases, both of them will provide correct information. However, for palmprints containing lots of

creases, the amount of white stripes will greatly increase, bringing much noise for the estimation algorithm. As a result, when the creases are overwhelming in a local region, the output of the above estimation algorithms will be wrong.

2.1 Main Procedure

In a police expert's experience, when he checks a latent palmprint, he will concentrate on the direction of black ridges, ignoring the disturbances of white stripes which are produced by creases. The expert would also consider the ridge orientation in the neighborhood while estimating the orientation field in a local area.

Following this experience, we propose a novel orientation estimation algorithm for palmprints. A new initial estimation method is developed to reliably estimate the orientation field even in regions having many creases. But its computational cost, like the Gabor-filter-bank-based method, is much higher than the traditional gradient-based and the DFT method. In order to reduce the computational cost, we develop a composite algorithm. In this algorithm, first, the creases in a palmprint are located; for the regions with few creases, the traditional method is employed, whereas the designed initial estimation method is used for the regions with many creases. This effectively combines the robustness of the novel and efficiency of the traditional methods. As a postsmoothing procedure, the region growing algorithm [8] is applied. A schematic diagram of the composite algorithm is shown in Fig. 2.

The first stage of the composite algorithm consists of estimation of ridge quality and determination of the initial estimation algorithm to be applied. In this stage, we use the crease extraction algorithm proposed in [6] to extract creases. In order to reduce the computational complexity, the image is divided into 16×16 pixel blocks and the crease features are computed for each of these blocks. The output of the crease extraction algorithm contains the crease orientation, I_D, and the crease energy, I_E. The crease orientation associated with a crease refers to the direction parallel to the crease, whereas crease energy corresponds to the width of the crease. The quality value for each block is computed as a sum of crease energy values for all of the creases present inside a 64×64 pixel neighboring region around the block under consideration.

The conventional DFT [8] method is applied for the blocks whose crease energy is smaller than a threshold. Here, we determine k most likely orientations of the block, denoted as $X = [X_1, X_2, \ldots, X_k]^T$, $X_i = (\theta_i, f_i)$, where θ_i is the ridge direction and f_i is the ridge density. Assuming that the ith peak in the frequency spectrum is at (u_i, v_i), then the corresponding candidate solution, $X_i = (\theta_i, f_i)$, is given by

$$\begin{cases} \theta_i = \arctan\frac{v_i}{u_i} - \frac{\pi}{2}, \\ f_i = \frac{\sqrt{u_i^2 + v_i^2}}{64}. \end{cases} \quad (1)$$

For the block with a large number of creases, a Radon-transform-based method (RTBM) is developed to focus on ridges and find out their directions, ignoring the disturbances from white stripes.

2.2 Radon-Transform-Based Orientation Estimation

For a pixel on the ridge, it should be a part of a low intensity stripe. As the ridge direction is slowly varying, a ridge can be approximated by a straight line in a local area. The Radon transform [27] is a robust method to detect lines in the image, which is defined as

$$R(r,\theta)[I(x,y)] = \sum_{x=0}^{W}\sum_{y=0}^{H} I(x,y)\delta(r - x\cos\theta - y\sin\theta), \quad (2)$$

where $I(x,y)$ is the gray level at the location (x,y), W is the image width, H is the image height, r is the vertical distance from the line to the origin, and θ is the inclination. Then, the problem of detecting lines is changed to voting for the best parameters.

Note that the original Radon transform is performed on the whole image, whereas we just want to search for ridges

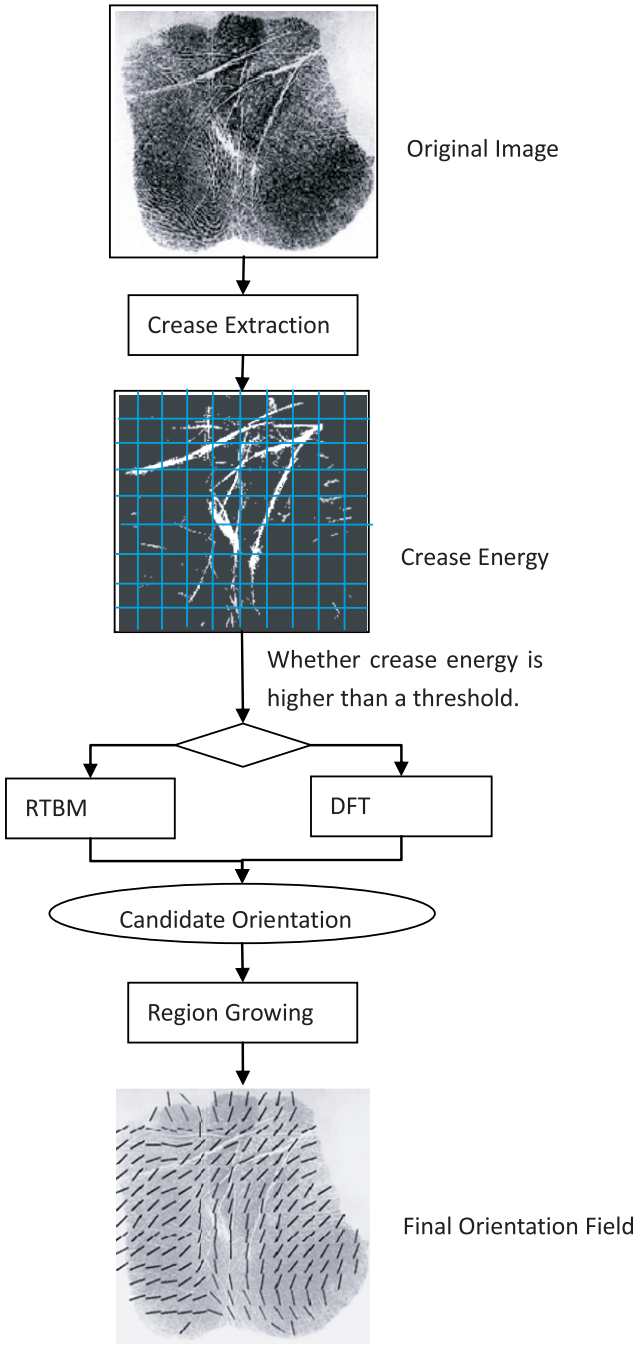

Fig. 2. The flowchart of the composite algorithm.

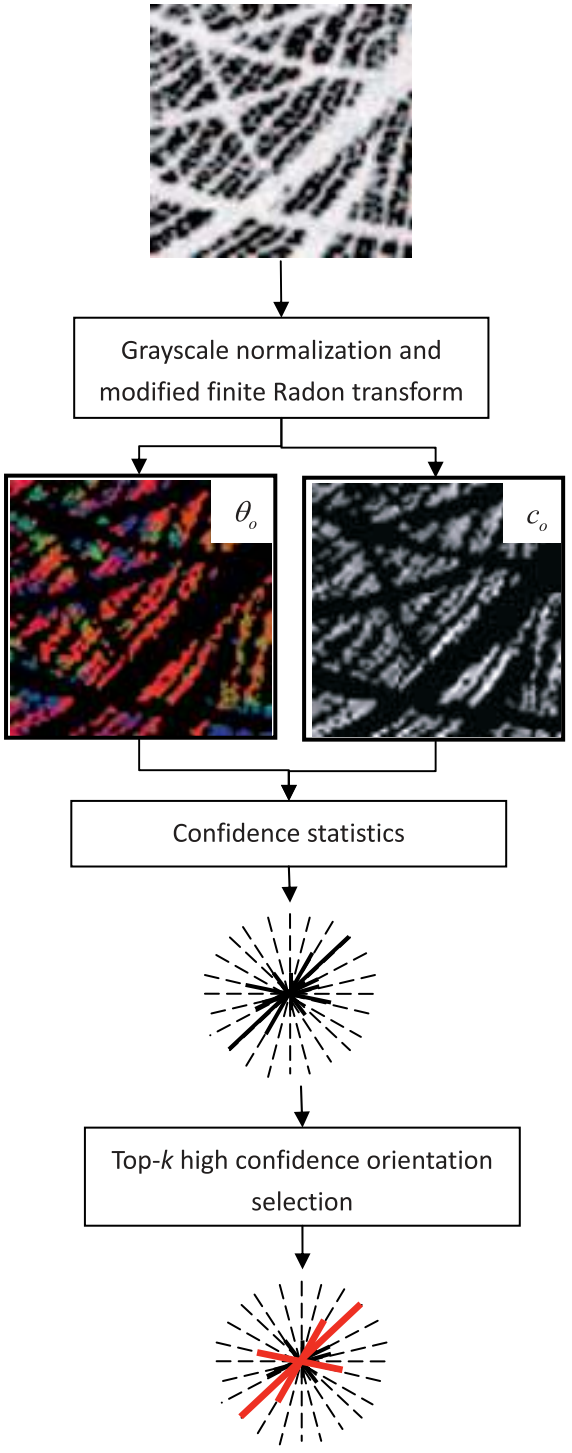

Fig. 3. The procedure of the proposed Radon-transform-based method. In the θ_0 image, the different directions are represented by different colors. For example, red, green, and blue represent 45, 120, and 165 degrees counterclockwise from the horizon, respectively. In the c_0 image, the confidence values are shown in different grayscales. For the confidence statistical result, the confidences of 12 directions are represented by their line lengths. The selected top-k high-confidence orientations are marked in red.

in a small local area. So, we utilize the modified finite Radon transform [6] to detect the ridge lines. The procedure of the proposed Radon-transform-based method is demonstrated in Fig. 3. First, all of the pixels in the current block's 64×64 pixel neighboring area Γ are scanned and those whose grayscales are lower than G_r are selected. Let the pixel at the location (x_0, y_0) be one of the selected pixels. Then, normalization is performed in a circular region Δ centered at (x_0, y_0) in the radius of 27 pixels by subtracting the mean of gray levels from every pixel. Next, the modified finite Radon transform is performed on Δ as

$$r(\theta; x_0, y_0) = \sum_{(x,y)\in\Delta} I(x,y)'\delta((x-x_0)\cos\theta + (y-y_0)\sin\theta), \tag{3}$$

where $I(x,y)'$ is the normalized gray level. In practice, the value of θ is discretized with $\pi/12$ as its minimum unit. The θ that minimizes $r(\theta; x_0, y_0)$, say θ_0, is picked out. And we associate a confidence value to the estimate given by

$$c_0(x_0, y_0) = -r(\theta_0; x_0, y_0). \tag{4}$$

To ascertain the coarse orientation of local ridge lines, the directions of the points in the block's 64×64 pixel neighboring area Γ should be taken into consideration. The respective aggregate confidence values of different directions are computed as

$$c_b(\varphi) = \sum_{(x,y)\in\Gamma} f(c_0(x,y))I(\theta_0(x,y) = \varphi), \tag{5}$$

where f is a nonlinear function. It takes the form of

$$f(c) = \begin{cases} 0, & \text{if } c \le c_T, \\ c, & \text{if } c > c_T, \end{cases} \tag{6}$$

where c_T is the truncation threshold and is empirically set as 200 in our experiment. This nonlinear function eliminates the effect of points that are highly unreliable, e.g., points near creases or points in a blurred or stained region.

Finally, the k directions with the top-k confidence values are considered as candidate ridge directions, and the ridge density extraction algorithm [28] is performed along the k directions separately.

2.3 Postsmoothing

Postsmoothing is used to correct the minor errors in the initial estimation result. As a postsmoothing procedure, we apply the region growing algorithm proposed by Jain and Feng in [8] in order to select the final orientation.

One of the main assumptions of the region growing algorithm is that the ridge direction and density are fixed in a local region. The region growing procedure is initialized at a set of seed points. To become a seed, the area should possess at least 20 connected blocks in which the adjacent blocks' first candidate solutions satisfy the continuity criterion. Two solutions, $X^a = (\theta^a, f^a)$ and $X^b = (\theta^b, f^b)$, are deemed to be continuous if

$$\begin{cases} |\theta^a - \theta^b| \le \frac{1}{6}\pi, \\ |1/f^a - 1/f^b| \le 3. \end{cases} \tag{7}$$

The next step is to grow from seeds and form regions. The four neighboring blocks of the current growing block are checked to find solutions continuous with the current block. Those blocks having continuous solutions with the current block are added to the region. Finally, regions

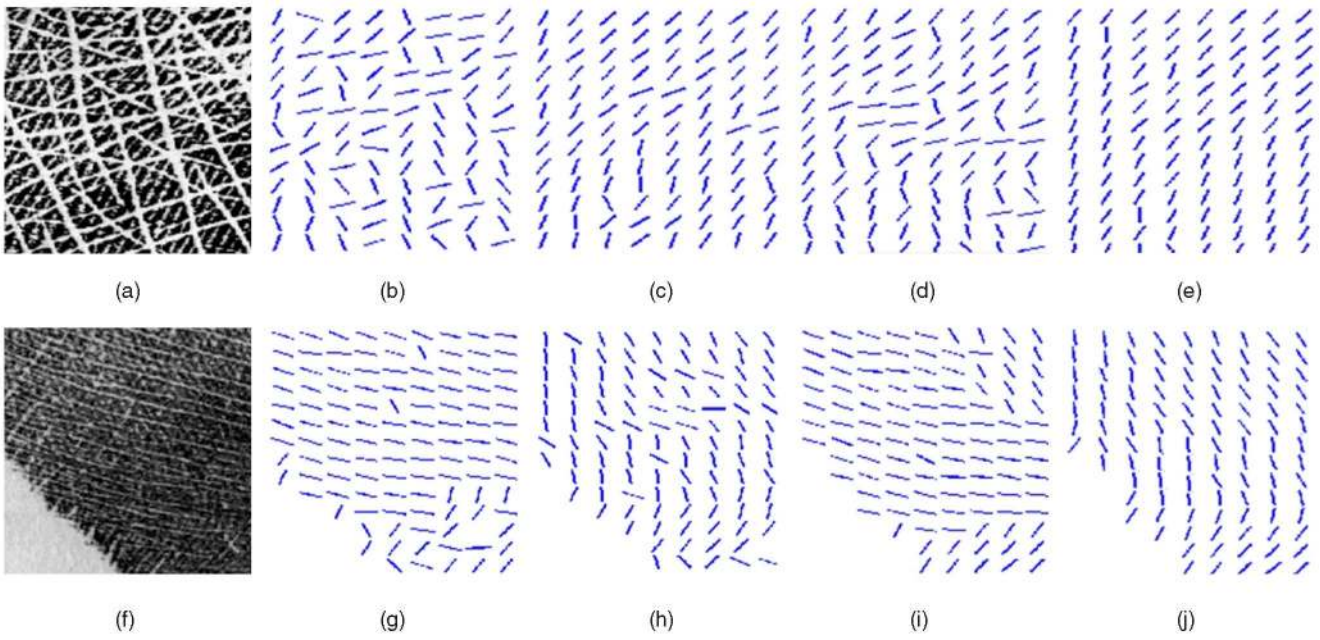

Fig. 4. Comparison of orientation field extraction: (a) and (f) are the original images, (b) and (g) are the initial orientation fields estimated by DFT, the initial estimation method in [8], (c) and (h) are the initial orientation fields produced by the Radon-transform-based method, (d) and (i) are the final orientation fields extracted by the algorithm of [8], and (e) and (j) are the final orientation fields produced by the proposed composite algorithm.

grown from different seeds are merged to form the final orientation field.

2.4 Computational Complexity

The computational cost of the composite algorithm varies with the amount of creases in the palmprint. Let $T_{Composite}$ be the time consumption of the composite algorithm, and then we have

$$T_{Composite} = T_{CreaseExtraction} + \alpha T_{RTBM} + (1-\alpha)T_{DFT} + T_{RegionGrowing}, \quad (8)$$

where $T_{CreaseExtraction}$ is the cost of crease extraction, T_{RTBM} is the time consumption of the RTBM, T_{DFT} is the cost of carrying out the DFT method, $T_{RegionGrowing}$ is the time performing region growing, and α is the proportion of blocks with heavy creases among all the blocks. In our experiments, for palmprints with enormous creases, α may reach 41 percent, while for those with little creases, α may be as low as 10 percent. For the palmprint database used in this paper, the average value of α is about 21 percent.

2.5 Comparison with the Orientation Estimation Algorithm in [8]

In this section, we compare the proposed composite algorithm with the orientation field estimation algorithm proposed in [8].

In [8], the initial orientation estimation is performed by the DFT method in 64×64 neighborhood. And the six waves with the strongest amplitude in the frequency domain of each block are used as candidates. Finally, the region growing algorithm selects the final orientation for each block from the candidates.

Compared with the algorithm in [8], the main difference of the proposed composite algorithm is in the initial estimation stage. Unlike the algorithm proposed in [8], we extract the quality of each image block and use it to select the appropriate initial estimation algorithm. We use the more robust Radon-transform-based method at the blocks with dense creases, while the DFT method is applied for the blocks with few creases.

Several comparisons between the proposed composite algorithm and the algorithm in [8] are shown in Fig. 4. Figs. 4a and 4f show two segments of palmprints with many creases. The resolution of these palmprints is 500 ppi, the same as that of the images in [8]. From Figs. 4c and 4h, we can see that the Radon transform-based initial estimation method can reliably extract the orientation field for the prints with many creases. And the result is much reliable than that of the DFT method, as shown in Figs. 4b and 4g. After postsmoothing, the final orientation field obtained by the proposed method is more accurate. Note that with more reliable orientation field, the following steps, such as minutiae extraction, are more effective. As a result, the whole recognition system's accuracy is improved, as shown in Section 5.2.

3 Feature Extraction

By using the composite algorithm, the orientation field can be reliably extracted. Now, we will introduce the extraction of minutiae, density map, and principal line map.

3.1 Minutiae

With reliable orientation field and density map information, a series of image processing steps can be performed to extract minutiae [24], [26], [29], [30]. First, the ridges are enhanced by the Gabor filter according to the local ridge direction and density. Second, the image is binarized and thinned to get the skeleton ridge image. Finally, minutiae are extracted as the endings and bifurcations points of ridge lines. The initial

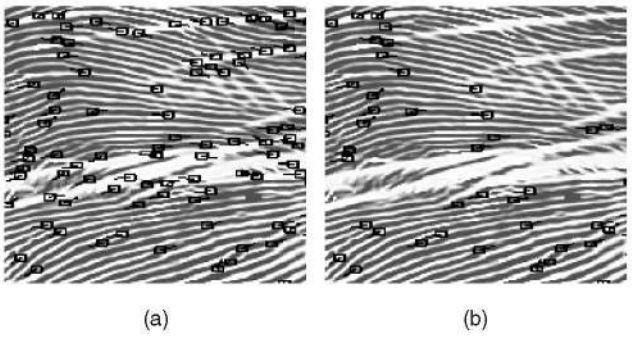

Fig. 5. Removal of spurious minutiae caused by creases: (a) before removal and (b) after removal.

minutiae set is denoted by $M = \{m_1, m_2, \ldots, m_n\}$, where $m_i = \{x_i, y_i, \theta_i\}$. x_i, y_i, and θ_i represent the ith minutia's x-coordinate, y-coordinate, and direction, respectively.

There are many spurious minutiae in the initial set, and a large portion of them are caused by creases. As creases cannot be fully removed by image enhancement, they will break the continuity of ridges and produce spurious minutiae. Since many creases are changeable with seasons and weathers [5], the resulting spurious minutiae are not robust.

The traditional method to remove the spurious minutiae caused by creases is to determine whether there are two minutia points with the same or opposite direction in a small neighboring area [26]. This procedure is based on the fact that creases are narrow, which is not valid for palmprints that have thick creases. Note that increasing the size of a neighboring area in order to accommodate thick creases will cause many genuine minutiae to be misclassified as imposter ones. The best way to remove the spurious minutiae is to make use of the crease information itself, which is extracted at the first step of the composite algorithm. If a minutia is close to a crease, then it is quite likely to be a spurious one. In our experiments, this method can effectively remove the spurious minutiae caused by creases. An example is shown in Fig. 5.

Next, the minutia's confidence level is evaluated based on the difference of the ridge direction produced by the composite algorithm and the gradient-based method in the region around the minutia. If the difference is high, the local image quality is poor and the confidence level associated with the minutia is low.

When matching two palmprint images, alignment should be performed as, usually, there is deformation between palmprints. The classic minutiae-based general Hough transform is applied to find the optimal transformation parameters [24].

The similarity of two sets of minutiae is computed as the product of matching quantity score S_{mn} and quality score S_{mq}. S_{mn} is measured by the sum of matched minutiae pairs' confidence level productions. S_{mq} is computed as the proportion of matched minutiae in all the minutiae within the common area. And the amount of minutiae in the common area for reference and query palmprints are defined to be the sum of the minutiae's confidence level on minutia extraction, which are denoted by C_r and C_q, respectively. The combined similarity score S_m from the minutiae feature is estimated as follows:

$$S_m = S_{mn} \times S_{mq} = \frac{C_p}{C_p + 20} \times \frac{C_p^2}{C_r C_q}, \tag{9}$$

where 20 is considered as the minimum value of C_p for genuine matches estimated on the training data set. This formulation reduces the effect of spurious minutiae on computation of matching scores.

3.2 Density Map

In our system, the density map is extracted simultaneously with the orientation field by using the composite algorithm. The similarity of the density map S_d is also defined as a product of matching quantity S_{fn} and quality S_{fq}. The matching quantity is measured by the number of matched block pairs. A matched block pair is comprised of two overlapped blocks whose ridge distance (the inverse of ridge density) difference is within 1 pixel. The matching quality reflects the average ridge distance differences of all of the blocks in the common area. The similarity score S_d is calculated as

$$\begin{aligned} S_d = S_{dn} \times S_{dq} = \frac{N_d}{N_d + 900} \\ \times \frac{1}{N_b} \sum_{(x,y)\in\Xi} \exp(-|1/f_r(x,y) - 1/f_q(x,y)|), \end{aligned} \tag{10}$$

where N_d is the number of matched blocks, 900 is the estimation of the minimum matched block numbers for genuine matches, Ξ denotes the common area, N_b is the number of blocks in the common area, and f_r and f_q denote the ridge densities of reference and query palmprints, respectively.

A similar formula is used to measure the similarity of the orientation field from two palmprints.

3.3 Principal Line Map

We need to further distinguish the principal lines from all of the detected creases. The general Hough transform [31] is applied to detect the principal lines. Let $w\cos\theta + h\sin\theta = r$ be the major axis of a candidate rectangular area corresponding to a principal line, and the general Hough transform is defined as

$$\begin{aligned} G(\theta, r) = \int_0^H \int_0^W I_E(w,h) I(|r - w\cos\theta - h\sin\theta| \\ < W/2) I(|I_D(w,h) - \theta| < \Psi) dw dh, \end{aligned} \tag{11}$$

where $I_E(w,h)$ and $I_D(w,h)$ are the crease energy and crease direction, respectively, Ψ and W are the thresholds of the direction and position difference, respectively, and I is the characteristic function whose value is 1 if the criterion is satisfied and 0 if not. In the experiment, W and Ψ were empirically set as 80 pixels and $\pi/6$, respectively.

Next, the strongest k peaks of the parameter space $\Theta \times R$ are obtained and are denoted by (θ_i, r_i) $(i = 1, 2, \ldots, k)$. These peaks correspond to k rectangular areas. The creases outside the rectangular areas are erased to form the principal line energy image I_E^P and the principal line direction image I_D^P. And in our experiment, k was empirically set as 5. The principal line points extracted are shown in Fig. 6d.

The similarity of principal line maps is measured by the proportion of matched principal line energy in all of the

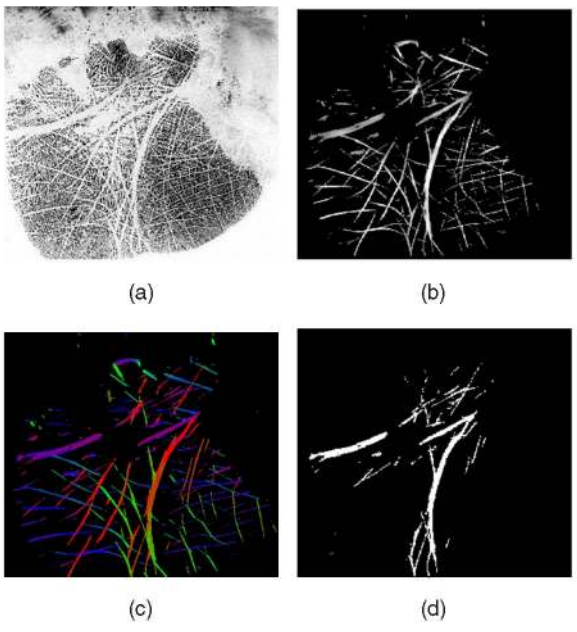

Fig. 6. Principal line map extraction: (a) a palmprint, (b) crease energy image, areas of higher grayscale have higher energy, (c) crease direction image, different crease directions are represented by different colors, and (d) extracted principal line map.

energy within the common area. Two energy points are deemed to be matched if they are located at the same position and the direction difference between their corresponding principal lines is less than $\pi/6$. The similarity is computed as

$$S_p = \frac{E_m}{\min\{E_r, E_q\}}, \tag{12}$$

where E_r and E_q are the principal line energy sum in the common area for reference and query palms, respectively, and E_m denotes the matched energy. It is calculated by

$$\begin{aligned} E_m = \sum_{(w,h)} & \min\{I_E^{P_r}(w,h), I_E^{P_q}(w,h)\} \\ & \cdot I\big(|I_D^{P_r} - I_D^{P_q}| \le \pi/6\big), \end{aligned} \tag{13}$$

where P_r and P_q denote the reference and query palmprints, respectively.

4 Multifeature Fusion

After the steps described, we get the matching scores of multiple features, including minutiae, orientation field, density map, and principal line map. In this section, we describe the techniques to combine them to measure the final similarity of two palmprints. Several fusion technologies have been proposed for the low-resolution palmprint recognition. Wang et al. [32] fused the palmprint image and palm vein image at the feature level. In [33], Kumar and Zhang fused multiple feature scores at the decision level and proposed a product of sum rule. In [34], Hennings-Yeomans et al. used the product rule for palmprint classification. Due to the differences in the nature of the application scenarios, we consider separate fusion techniques for verification and identification. For verification, we use some conventional statistical learning methods for the classification of the genuine and imposter matches. For identification, a novel heuristic rule is proposed to achieve a higher identification rate.

4.1 Statistical Methods for Verification

Given the similarity scores of various features between two palmprints, the verification system should decide whether they are from the same palm. The performance of verification is usually evaluated using the curve of the Receiver Operating Characteristic (ROC), which is a graph of FRR versus FAR. The simplest fusion technique is to compute the linear weighted sum of all of the similarity scores $S = \sum_i^k w_i S_i$ and set a threshold S_T. If S is higher than S_T, it is deemed a genuine match or else an imposter one. This is equivalent to separating two classes by a hyperplane in the feature space. But in most cases, the genuine and imposter matches are not linearly separable.

In order to accommodate nonlinearly separable densities, we learn the probability that a given match S^* is genuine $P(G|S^*)$ or imposter $P(I|S^*)$ and use a threshold-based classification for the two densities. Here, G denotes the genuine scores and I denotes the impostor scores. Examples of such techniques include SVMs [35] and the Neyman-Pearson rule [36].

SVMs have two basic advantages: First, the kernel techniques can be used to convert nonlinearly separable densities into a pair of linearly separable ones, and second, SVMs minimize the maximum expected generalization error, leading to good generalization ability [37].

As for the Neyman-Pearson rule, supposing the genuine class-conditional density is denoted by $P(S|G)$ and the imposter class-conditional density is denoted by $P(S|I)$, the classification criterion is given by

$$S \in \begin{cases} G, & \text{if } \mathrm{P(S|G)} > \lambda \mathrm{P(S|I)}, \\ I, & \text{if } \mathrm{P(S|G)} \le \lambda \mathrm{P(S|I)}. \end{cases} \tag{14}$$

To estimate the class-conditional density distributions $P(S|G)$ and $P(S|I)$, the Parzen window method is applied. And Gaussian kernel is used as the window function

$$\hat{P}_N(x) = \frac{1}{N}\sum_{i=1}^{N} \frac{1}{V_N}\varphi\left(\frac{x - x_i}{h_N}\right), \tag{15}$$

where $\varphi(u) = \frac{1}{\sqrt{2\pi}}\exp(-\frac{1}{2}u^2)$, x_i is the similarity vector of the ith training sample, N is the number of training samples, h_N is the window width, $V_N = h_N^d$, and d is the dimension of x.

4.2 A Heuristic Rule for Identification

In an identification task, given a query palmprint, it is compared with all of the palmprints in the database and they are ranked according to their similarities to the query palmprint in descending order. The performance of identification is usually evaluated by the identification rate, which is defined as the probability that the identified palmprint can be ranked within the top-k candidates. A graph showing the identification rates for different values of k is called a Cumulative Match Curve (CMC). Although the CMC and ROC curves are very relevant, the optimization goals of verification and identification are quite different [38]. So the best fusion methods for verification,

such as SVMs and Neyman-Pearson methods, are not optimal for identification tasks. The weighted sum rule performs well when different features are conditionally independent, but its performance deteriorates if some features are conditionally correlated [39]. For our study, the minutiae and orientation field features are heavily correlated as the ridge direction information is embedded into them simultaneously. To improve the system's performance, a novel heuristic rule is developed by analyzing the characteristics and correlations of different features.

As minutiae and density map features are of low correlation and have comparable discriminative power, they can be fused by the weighted sum rule as

$$S_{md} = w_m S_m + (1 - w_m) S_d, \tag{16}$$

where S_m, S_d are the matching scores of minutiae and density map, respectively. The weight w_m is evaluated at the training set and empirically set as 0.65.

In the case of the principal line map, although its discriminative power is worse than the other features, it can provide independent global information of the palmprint. In the experiment, many genuine and imposter matches have similar low-similarity scores. But we also find that only genuine matches can reach high similarity scores. So, if the matching score of the principal line map is low, its influence on the final result should be weak and the decision should be primarily based on the information provided by the other features. But in case two palmprints' principal line maps are very similar, the rule should assert that they are quite likely to be from the same palm. Let S_p be the matching score of the principal line, then the similarity score of the above three features, S_{mdp}, is calculated by

$$S_{mdp} = S_{md} + S_{md} \times \frac{1}{1 - S_p}. \tag{17}$$

When S_p is low, the result is mainly influenced by the similarity of minutiae and density map. However, when S_p is close to 1, the value of $\frac{1}{1-S_p}$ is high, and it will add a lot to the matching score.

As for the orientation field, its discriminative power is not good for palmprint recognition because many palms have similar ridge direction patterns. The information of the orientation field is heavily correlated with minutiae since the direction of minutia fully captures the ridge orientation at that point. In [40], Chen et al. reconstructed the orientation field by using minutiae information and achieved a satisfying result, which also proved the above conclusion. So the rule should mainly rely on the information provided by the other features. If the similarity of the other features is low, the overall similarity should be low. Otherwise, the similarity of the orientation field, S_o, can be taken into consideration. Considering these factors, the overall similarity is defined as

$$S = S_{mdp} + S_{mdp} \times S_o. \tag{18}$$

5 Experimental Results

In this section, we describe the database and details of the specific experiments which include the following:

TABLE 1
Summary of the THUPALMLAB Database

Print type		No. of palmprints	No. of palms
Partial palmprint	From hypothenar region	240	120
	From thenar region	240	
	From interdigital region	240	
Full palmprint	Multiple print	960	
	Single print	13,616	13,616

1. comparison between different orientation field estimation algorithms,
2. analysis of different feature combinations,
3. analysis of different fusion methods,
4. comparison with the previous algorithm.

5.1 Palmprint Database

Up to now, there has been no publicly available high-resolution palmprint database. To test the algorithm, we built a large-scale palmprint database containing 14,576 full palmprints from 13,736 palms, which is referred to as THUPALMLAB. The database's size is much larger than the database used in [8]. The image size is $2{,}040 \times 2{,}040$ pixels with 500 ppi resolution and 256 grayscales. The database contains both full and partial palmprints. The set of full palmprints consists of two parts; 120×8 of them are collected from 120 different palms by using a Hisign palm scanner. During the image acquisition, we did not guide the subjects to simulate the real situations and each palm was pressed eight times. The remaining 13,616 palmprints are inked images provided by the Forensic Science Department of the Chinese Police, which are from 13,616 different palms, one print for each palm. These 13,616 palmprints were scanned at the same resolution as the live scanned images. To simulate the latents recovered from crime scenes, we scanned partial palmprints from different regions of the palms, following the method in [8]. For each of the first 120 palms, two partial prints are scanned from the thenar, hypothenar, and interdigital regions of the first two presses, respectively. As a result, we collected 120×6 partial palmprints from 120 unique palms. Among all of the palmprint images, about 17 percent of them are of relatively poor quality due to large amounts of creases, deformity, smudges, blurs, incompleteness, etc. The database is summarized in Table 1 and some of the sample images are shown in Fig. 7.

In experiments, we specified the palmprints from 40 palms with multiple prints as the training set. All of the remaining palmprints, including 80×8 multiple prints, 80×6 partial prints, and 13,616 single prints, form the test set. In the verification experiment, the 80×8 multiprint and 13,616 single print full palmprints from the test set are matched with each other, leading to 2,240 genuine and 600,000 imposter matches. In the identification experiment, the 80×6 partial palmprints are used as query palmprints and 80 full palmprints from the corresponding third impressions are mixed with the 13,616 single print palmprints to form the background database.

5.2 Comparison between Different Orientation Field Estimating Algorithms

We compared the composite orientation estimation algorithm with the orientation estimation algorithm in [8]. Two

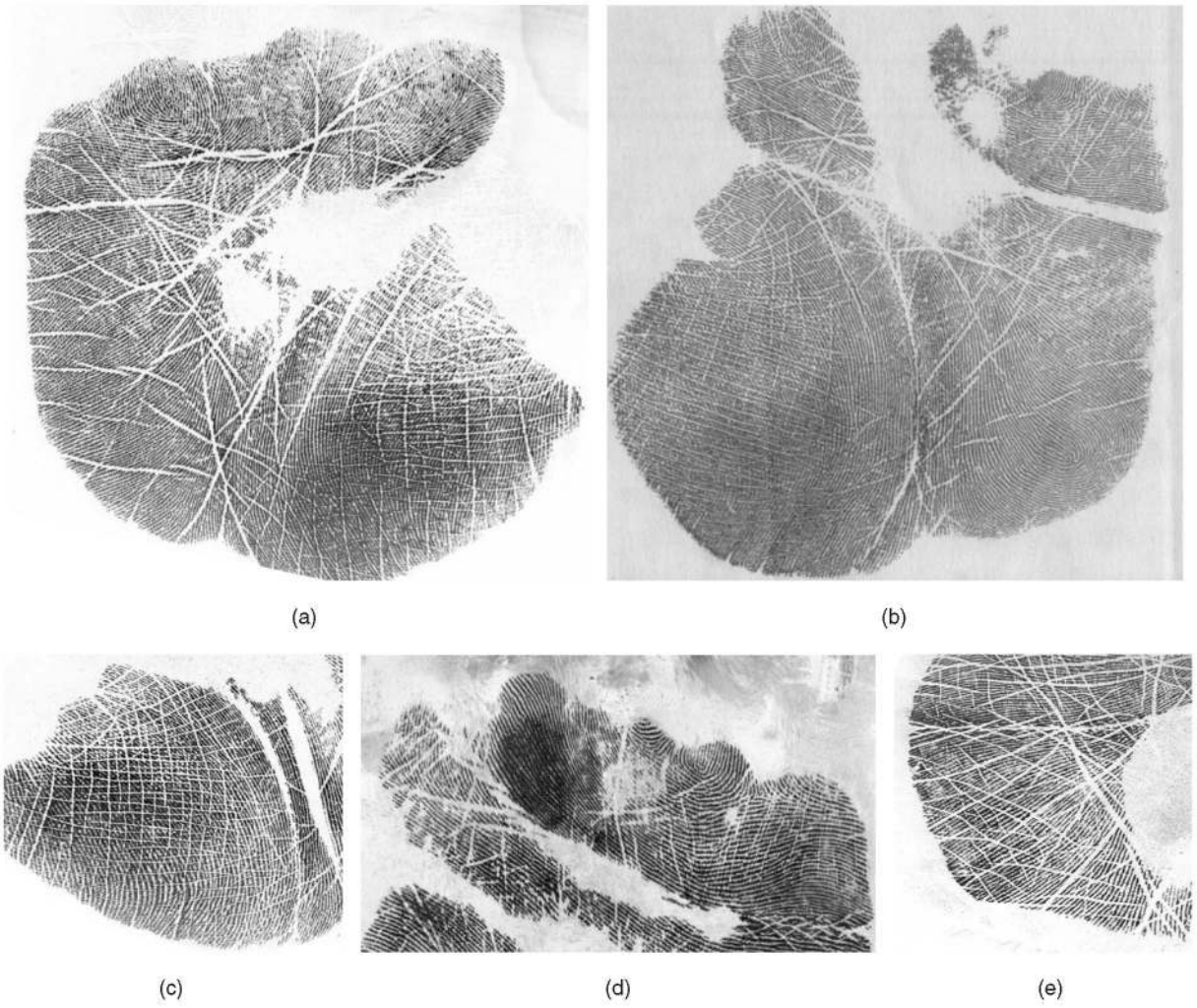

Fig. 7. Sample palmprint images from the THUPALMLAB database: (a) live-scanned full palmprint image, (b) inked full palmprint image, (c)-(e) partial palmprints.

recognition systems were built. One uses the proposed algorithm, the other uses the algorithm in [8], and all of the other techniques used for evaluation, etc., are exactly the same. The matching is done by combining the decisions of classifiers based on minutiae and orientation field as in [8]. We tested the two systems' performance both by verification and identification experiments, and the corresponding ROC and CMC curves are shown in Fig. 8, respectively.

As shown in Fig. 8, the system using the proposed orientation estimation algorithm has better performance in both the verification and identification experiments. The main factor contributing to the improved performance is the highly reliable orientation field extraction procedure. As the ridge direction and density information are necessary for minutiae extraction, minutiae thus obtained are also more reliable.

5.3 Discriminative Power of Different Feature Combinations

The discriminative power of different feature combinations is compared for verification and identification usages, respectively. The features in decreasing order of discriminative power are minutiae, density map, orientation field, and principal line map. Unlike fingerprints, the discriminatory power of the density map is greater than that of the orientation field. The reasons lie in the following aspects: First, the ridge distances of palmprints are in a much larger range, which is 8 to 13 pixels. Besides, the ridge distances of different palms in the same region (e.g., thenar) have a larger difference. In the case of orientation field, the ridge directions are quite similar for different palms in the same region. Fig. 9 shows two palmprints from different palms having similar orientation field patterns. However, their ridge density distributions are quite different, as shown in Figs. 9e and 9f.

We analyzed the increase in discriminative power when minutiae are combined with the other features, since minutiae is the most important feature and the alignment is based on minutiae information. The features are fused by the SVMs for verification and by the weighted sum rule for identification. For the SVMs, we used the RBF kernel and set $C = 10$, $\gamma = 10, 6, 3$ for combining 2, 3, 4 features, respectively. The ROC and CMC curves are shown in Fig. 10. As shown in Fig. 10, incorporating just the density map leads to similar improvement as the case when all of the additional features are used. This is because both the minutiae and density map have good discriminative power and are highly

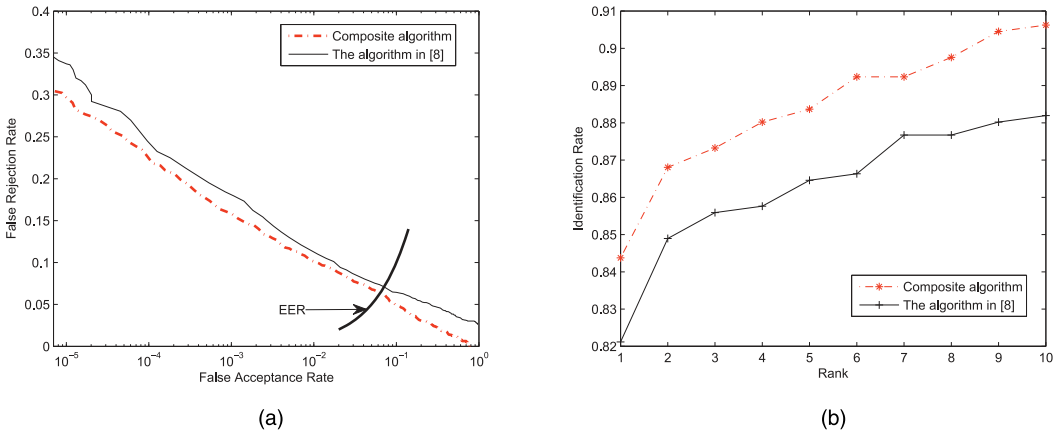

Fig. 8. The ROC and CMC curves of the proposed composite orientation estimation algorithm and the algorithm in [8] on THUPALMLAB: (a) ROC curves and (b) CMC curves.

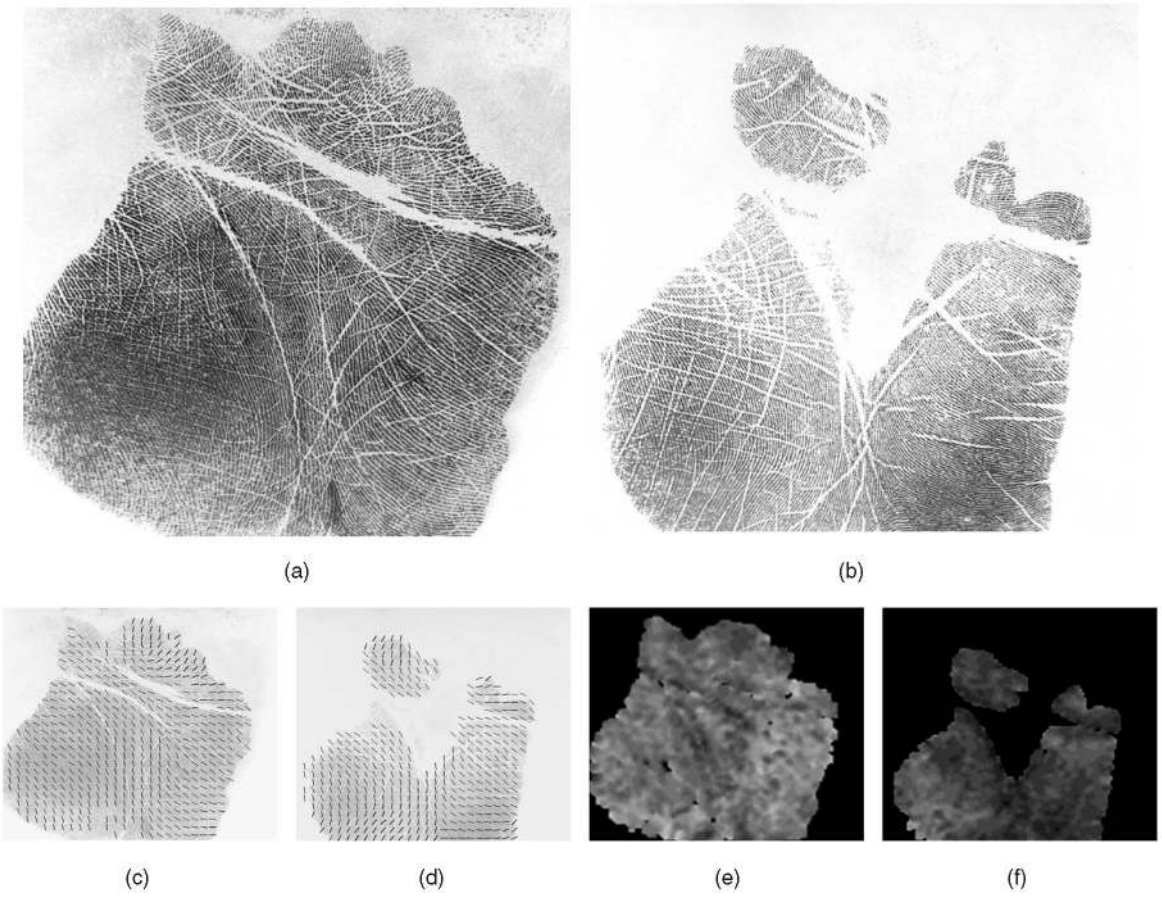

Fig. 9. Two palmprints from different subjects with similar orientation field but diverse density map patterns: (a), (b) original palmprint images, (c), (d) orientation fields, (e), (f) density maps. In the density map images, the grayscale value is proportional to the ridge density.

independent, while we can find that although the accuracy of only using orientation field is much higher than that of principal line map, the discriminative power of their combinations with minutiae is almost the same in verification. And in identification test, although the combination of minutiae and orientation field has higher top-1 and top-2 identification rate, the combination of minutiae and principal line map outperforms it in the top-3 identification rate. When combining two additional features with minutiae, the combination of minutiae, density map, and principal line map shows better performance than that of minutiae, density map, and orientation field in both verification and identification tests. That is because the correlation between the orientation field and minutiae is strong, whereas that between the principal line map and minutiae is relatively weak. The above conclusions can also be drawn when using the other data fusion methods.

5.4 Comparison between Different Fusion Methods

We compared the performance of different fusion methods, including weighted sum rule, SVMs, Neyman-Pearson rule, and the proposed heuristic rule. The parameters are computed on the training set for both verification and identification. The SVMs uses the RBF kernel and the

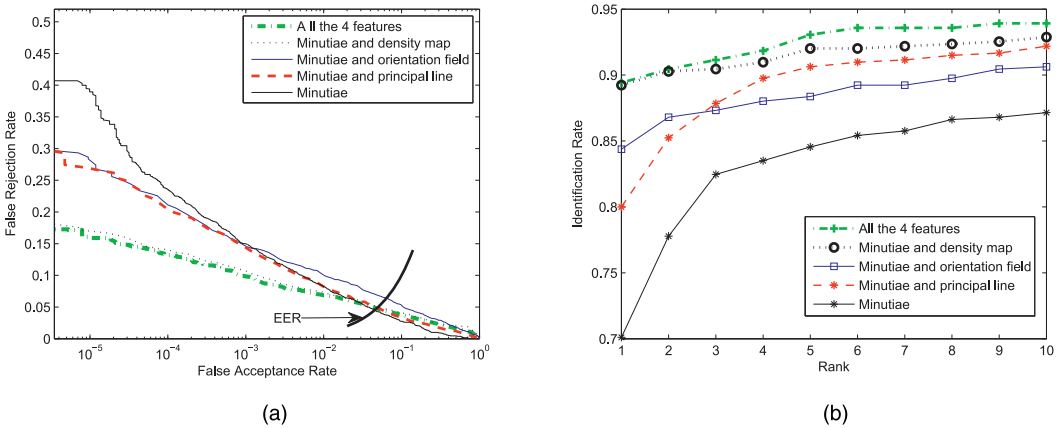

Fig. 10. The ROC and CMC curves of the combinations of minutiae and additional features on THUPALMLAB: (a) ROC curves and (b) CMC curves.

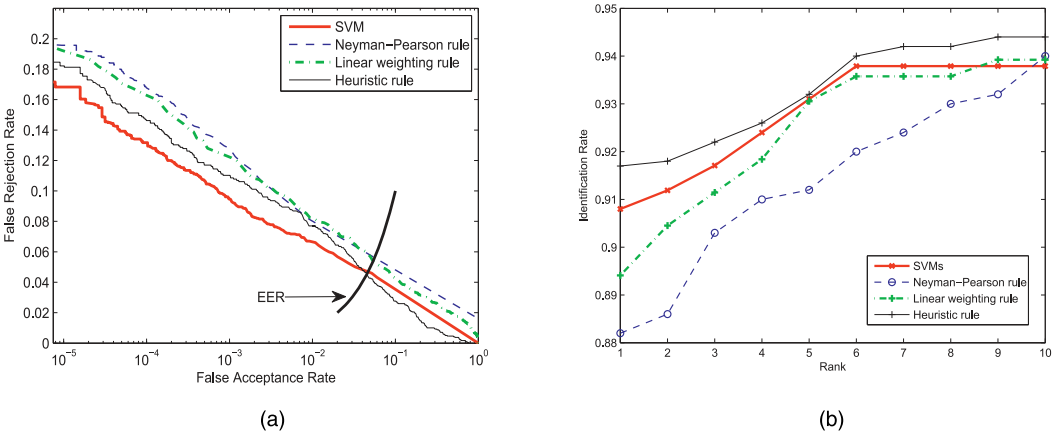

Fig. 11. The ROC and CMC curves of classifiers using weighted sum rule, SVMs, Neyman-Pearson rule, and the proposed heuristic rule on THUPALMLAB: (a) ROC curves and (b) CMC curves.

parameters are set as $C = 10, \gamma = 10$ and $C = 7, \gamma = 8$ for verification and identification, respectively. In the case of the Neyman-Pearson rule, h_N is set as 0.07 and 0.08 in the verification and identification tests, respectively. The parameters of the heuristic rule are described in Section 4.2. And the weighted sum rule is given as

$$S = 0.53S_m + 0.28S_d + 0.10S_o + 0.10S_p. \quad (19)$$

These weights are also estimated using the training set.

Next, recognition systems were built using different fusion methods to combine the four features, while keeping all of the other parts the same. Their performances in verification and identification experiments on THUPALMLAB are shown in Fig. 11.

In the verification experiment, fusion by the SVMs can get more accurate results than the other three methods. And the performance of the Neyman-Pearson rule, the weighted sum rule, and the proposed heuristic rule is similar, while in the identification experiment, the result is quite different and the proposed heuristic rule shows a best performance.

5.5 Comparison with Previous Works

We compared our algorithm with Jain and Feng's algorithm [8] on the THUPALMLAB. Based on the above analysis, we select the SVMs as the fusion method for the verification system and the proposed heuristic rule for the identification system.

Fig. 12a shows the FRR obtained by the proposed approach is 16 percent, which is 17 percent lower than that obtained using the approach proposed in [8] at a FAR of 10^{-5}. The Equal Error Rate (EER) values of the proposed approach and the approach in [8] are 4.8 percent and 7.0 percent, respectively. Fig. 12b shows the CMC curves of identification experiment. Our technique achieves a rank-1 identification rate of 91.7 percent, which is 9.7 percent higher than that using the approach in [8]. About 94.3 percent of the corresponding palms can be found in the top-10 candidates using our approach. Both of the experiments indicate that the proposed algorithm achieves much better performance than the previous algorithm.

Performance improvement is mainly because of the following three reasons: 1) Multiple features, including minutiae, orientation field, density map, and principal line map, are utilized to provide more discriminative information, 2) the composite algorithm can estimate the orientation field more reliably in the case of regions with dense creases, and 3) the statistical learning method and the proposed heuristic rule are employed for verification and identification, respectively, to make better use of the multiple features.

6 Conclusions

In this paper, we developed a novel high-resolution palmprint recognition system which can handle palmprints

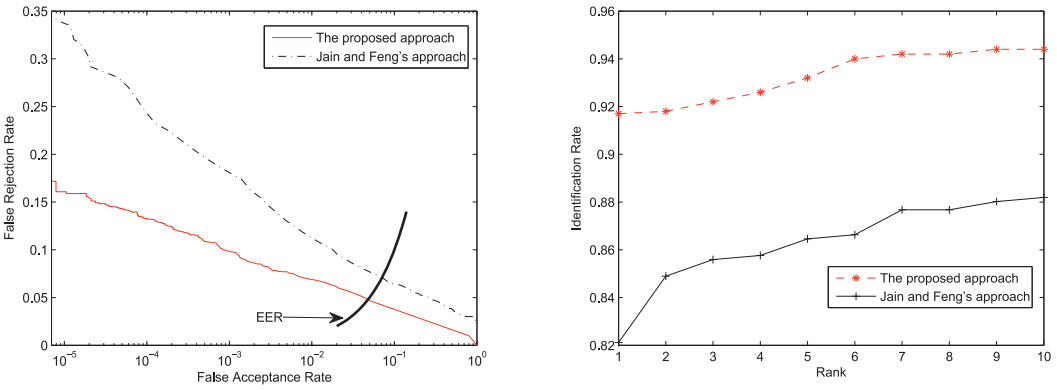

Fig. 12. The ROC and CMC curves of the proposed algorithm and the previous algorithm on THUPALMLAB: (a) ROC curves and (b) CMC curves.

with a large amount of creases, leading to much higher accuracy than the previous systems. The main contributions are as follows:

First, use of multiple features for palmprint recognition to significantly improve the matching accuracy.

Second, design of a quality-based and adaptive orientation field estimation algorithm. It can reliably estimate the ridge direction by adaptively choosing suitable estimation method according to the image quality.

Third, use of a novel heuristic rule for identification applications to combine different features.

Fourth, the discriminative power of different feature combinations is analyzed and we find that density is very useful for palmprint recognition.

We argue that further research on palmprint recognition should focus on handling nonlinear deformation and matching efficiency. Relative nonlinear deformation among different impressions of the same palm is unavoidable in the case of a contact-based scanner. And this significantly affects the matching of minutiae, orientation, and density map, especially in the case of palmprints that have much larger size as compared to fingerprints. Another challenge for high resolution palmprint recognition is fast matching in a large-scale database. A better indexing and searching method should be studied.

Acknowledgments

The authors would like to thank Dr. Abhishek Nagar and Dr. Jianjiang Feng for their help in revising this paper. This work was supported by the National 863 Hi-Tech Development Program of China under Grant 2008AA01Z123, by the Nation Science Foundation of China under Grants 61020106004, 60875017, 61005023, and 61021063, and by the Natural Science Foundation of Beijing under Grant 4042020.

References

[1] A. Jain, P. Flynn, and A. Ross, *Handbook of Biometrics.* Springer, 2007.
[2] S. Dewan and W. Elementary, "Scan a Palm, Find a Clue," *The New York Times,* 2003.
[3] *The FBIs Next Generation Identification(NGI),* http://fingerprint.nist.gov/standard/Presentations/archives/NGI_Overview_Feb_2005.pdf, 2009.
[4] F. Galton, *Fingerprints.* Wm. S. Hein Publishing, 2002.
[5] J. Zhou, F. Chen, N. Wu, and C. Wu, "Crease Detection from Fingerprint Images and Its Applications in Elderly People," *Pattern Recognition,* vol. 42, no. 5, pp. 896-906, 2009.
[6] D. Huang, W. Jia, and D. Zhang, "Palmprint Verification Based on Principal Lines," *Pattern Recognition,* vol. 41, no. 4, pp. 1316-1328, 2008.
[7] D. Ashbaugh, *Quantitative-Qualitative Friction Ridge Analysis: An Introduction to Basic and Advanced Ridgeology.* CRC Press, 1999.
[8] A. Jain and J. Feng, "Latent Palmprint Matching," *IEEE Trans. Pattern Analysis and Machine Intelligence,* vol. 31, no. 7, pp. 1032-1047, July 2009.
[9] D. Zhang, W. Kong, J. You, and M. Wong, "Online Palmprint Identification," *IEEE Trans. Pattern Analysis and Machine Intelligence,* vol. 25, no. 9, pp. 1041-1050, Sept. 2003.
[10] W. Kong, D. Zhang, and W. Li, "Palmprint Feature Extraction Using 2-D Gabor Filters," *Pattern Recognition,* vol. 36, no. 10, pp. 2339-2347, 2003.
[11] A. Kong and D. Zhang, "Competitive Coding Scheme for Palmprint Verification," *Proc. 17th Int'l Conf. Pattern Recognition,* vol. 1, 2004.
[12] A. Kong, D. Zhang, and M. Kamel, "Palmprint Identification Using Feature-Level Fusion," *Pattern Recognition,* vol. 39, no. 3, pp. 478-487, 2006.
[13] A. Kumar and D. Zhang, "Personal Recognition Using Hand and Texture," *IEEE Trans. Image Processing,* vol. 15, no. 8, pp. 2454-2461, Aug. 2006.
[14] W. Jia, D. Huang, and D. Zhang, "Palmprint Verification Based on Robust Line Orientation Code," *Pattern Recognition,* vol. 41, no. 5, pp. 1521-1530, 2008.
[15] W. Shu and D. Zhang, "Automated Personal Identification by Palmprint," *Optical Eng.,* vol. 37, no. 8, pp. 2359-2362, 1998.
[16] D. Zhang and W. Shu, "Two Novel Characteristics in Palmprint Verification: Datum Point Invariance and Line Feature Matching," *Pattern Recognition,* vol. 32, no. 4, pp. 691-702, 1999.
[17] N. Duta, A. Jain, and K. Mardia, "Matching of Palmprints," *Pattern Recognition Letters,* vol. 23, no. 4, pp. 477-486, 2002.
[18] J. You, W. Li, and D. Zhang, "Hierarchical Palmprint Identification via Multiple Feature Extraction," *Pattern Recognition,* vol. 35, no. 4, pp. 847-859, 2002.
[19] C. Harris and M. Stephens, "A Combined Corner and Edge Detector," *Proc. Alvey Vision Conf.,* vol. 15, p. 50, 1988.
[20] Z. Sun, T. Tan, Y. Wang, and S. Li, "Ordinal Palmprint Represention for Personal Identification," *Proc. IEEE CS Conf. Computer Vision and Pattern Recognition,* vol. 1, pp. 279-284,
[21] F. Yue, W. Zuo, D. Zhang, and K. Wang, "Orientation Selection Using Modified FCM for Competitive-Based Palmprint Recognition," *Pattern Recognition,* vol. 42, no. 11, pp. 2841-2849, 2009.
[22] A. Kumar, "Incorporating Cohort Information for Reliable Palmprint Authentication," *Proc. Sixth Indian Conf. Computer Vision, Graphics and Image Processing,* pp. 583-590, 2008.
[23] J. Travis, "Forensic Friction Ridge (Fingerprint) Examination Validation Studies," 2000.

[24] A. Jain, L. Hong, and R. Bolle, "On-Line Fingerprint Verification," *IEEE Trans. Pattern Analysis and Machine Intelligence,* vol. 19, no. 4, pp. 302-314, Apr. 1997.
[25] A. Jain, S. Prabhakar, and L. Hong, "A Multichannel Approach to Fingerprint Classification," *IEEE Trans. Pattern Analysis and Machine Intelligence,* vol. 21, no. 4, pp. 348-359, Apr. 1999.
[26] J. Zhou and J. Gu, "A Model-Based Method for the Computation of Fingerprints' Orientation Field," *IEEE Trans. Image Processing,* vol. 13, no. 6, pp. 821-835, June 2004.
[27] J. Radon, "Uber die Bestimmung von Funktionen durch Ihre Integralwerte Langs Gewisser Mannigfaltigkeiten," *Berichte Sachsische Akademie der Wissenschaften,* vol. 29, pp. 262-277, 1917.
[28] D. Wan and J. Zhou, "Fingerprint Recognition Using Model-Based Density Map," *IEEE Trans. Image Processing,* vol. 15, no. 6, pp. 1690-1696, June 2006.
[29] N. Ratha, K. Karu, S. Chen, and A. Jain, "A Real-Time Matching System for Large Fingerprint Databases," *IEEE Trans. Pattern Analysis and Machine Intelligence,* vol. 18, no. 8, pp. 799-813, Aug. 1996.
[30] D. Maltoni, A. Jain, and S. Prabhakar, *Handbook of Fingerprint Recognition.* Springer, 2009.
[31] D. Ballard, "Generalizing the Hough Transform to Detect Arbitrary Shapes," *Pattern Recognition,* vol. 13, no. 2, pp. 111-122, 1981.
[32] J. Wang, W. Yau, A. Suwandy, and E. Sung, "Person Recognition by Fusing Palmprint and Palm Vein Images Based on Laplacian-palm Representation," *Pattern Recognition,* vol. 41, no. 5, pp. 1531-1544, 2008.
[33] A. Kumar and D. Zhang, "Personal Authentication Using Multiple Palmprint Representation," *Pattern Recognition,* vol. 38, no. 10, pp. 1695-1704, 2005.
[34] P. Hennings-Yeomans, B. Kumar, and M. Savvides, "Palmprint Classification Using Multiple Advanced Correlation Filters and Palm-Specific Segmentation," *IEEE Trans. Information Forensics and Security,* vol. 2, no. 3, pp. 613-622, Sept. 2007.
[35] C. Cortes and V. Vapnik, "Support-Vector Networks," *Machine Learning,* vol. 20, no. 3, pp. 273-297, 1995.
[36] S. Prabhakar and A. Jain, "Decision-Level Fusion in Fingerprint Verification," *Pattern Recognition,* vol. 35, no. 4, pp. 861-874, 2002.
[37] J. Suykens and J. Vandewalle, "Least Squares Support Vector Machine Classifiers," *Neural Processing Letters,* vol. 9, no. 3, pp. 293-300, 1999.
[38] R. Bolle, J. Connell, S. Pankanti, N. Ratha, and A. Senior, "The Relation between the ROC Curve and the CMC," *Proc. Fourth IEEE Workshop Automatic Identification Advanced Technologies,* pp. 15-20, 2005.
[39] J. Kitler, M. Hatef, R. Duin, and J. Matas, "On Combining Classifiers," *IEEE Trans. Pattern Analysis and Machine Intelligence,* vol. 20, no. 3, pp. 226-239, Mar. 1998.
[40] F. Chen, J. Zhou, and C. Yang, "Reconstructing Orientation Field from Fingerprint Minutiae to Improve Minutiae-Matching Accuracy." *IEEE Trans. Image Processing,* vol. 18, no. 7, pp. 1665-1670, July 2009.

Jifeng Dai received the BS degree from Tsinghua University, Beijing, China, in 2009. Currently, he is working toward the PhD degree in the Department of Automation, Tsinghua University. His research interests include pattern recognition, computer vision, and machine learning.

Jie Zhou received the BS and MS degrees from the Department of Mathematics, Nankai University, Tianjin, China, in 1990 and 1992, respectively, and the PhD degree from the Institute of Pattern Recognition and Artificial Intelligence, Huazhong University of Science and Technology (HUST), Wuhan, China, in 1995. From 1995 to 1997, he was a postdoctoral fellow with the Department of Automation, Tsinghua University, Beijing, China. Currently, he is a full professor with the Department of Automation, Tsinghua University. His research interests include pattern recognition, computer vision, and data mining. In recent years, he has authored more than 100 papers in peer-reviewed international journals and conferences. He received the Best Doctoral Thesis Award from HUST in 1995, the First Class Science and Technology Progress Award from the Ministry of Education (MOE) in 1998, the Excellent Teaching Award from Tsinghua University in 2003, and the Best Advisor Award from Tsinghua University in 2004 and 2005. He was selected as one of the outstanding scholars of MOE in 2005. He is an associate editor for the *International Journal of Robotics and Automation* and *Acta Automatica Sinica*. He is a senior member of the IEEE.